remote sensing

MDPI

Article

Enhancing Georeferencing and Mosaicking Techniques over Water Surfaces with High-Resolution Unmanned Aerial Vehicle (UAV) Imagery

Alejandro Román [1,*], Sergio Heredia [1], Anna E. Windle [2,3], Antonio Tovar-Sánchez [1] and Gabriel Navarro [1]

[1] Department of Ecology and Coastal Management, Institute of Marine Sciences of Andalusia (ICMAN-CSIC), Spanish National Research Council (CSIC), 11510 Puerto Real, Spain; sergio.h.c@csic.es (S.H.); a.tovar@csic.es (A.T.-S.); gabriel.navarro@icman.csic.es (G.N.)
[2] NASA Goddard Space Flight Center, Greenbelt, MD 20771, USA; anna.windledipaola@nasa.gov
[3] Science Systems and Applications Inc., Lanham, MD 20706, USA
* Correspondence: a.roman@csic.es

Abstract: Aquatic ecosystems are crucial in preserving biodiversity, regulating biogeochemical cycles, and sustaining human life; however, their resilience against climate change and anthropogenic stressors remains poorly understood. Recently, unmanned aerial vehicles (UAVs) have become a vital monitoring tool, bridging the gap between satellite imagery and ground-based observations in coastal and marine environments with high spatial resolution. The dynamic nature of water surfaces poses a challenge for photogrammetric techniques due to the absence of fixed reference points. Addressing these issues, this study introduces an innovative, efficient, and accurate workflow for georeferencing and mosaicking that overcomes previous limitations. Using open-source Python libraries, this workflow employs direct georeferencing to produce a georeferenced orthomosaic that integrates multiple UAV captures, and this has been tested in multiple locations worldwide with optical RGB, thermal, and multispectral imagery. The best case achieved a Root Mean Square Error of 4.52 m and a standard deviation of 2.51 m for georeferencing accuracy, thus preserving the UAV's centimeter-scale spatial resolution. This open-source workflow represents a significant advancement in the monitoring of marine and coastal processes, resolving a major limitation facing UAV technology in the remote observation of local-scale phenomena over water surfaces.

Keywords: drones; mosaic; stitching; remote sensing; multispectral; RGB; thermal; water surfaces; water quality; georeference

Citation: Román, A.; Heredia, S.; Windle, A.E.; Tovar-Sánchez, A.; Navarro, G. Enhancing Georeferencing and Mosaicking Techniques over Water Surfaces with High-Resolution Unmanned Aerial Vehicle (UAV) Imagery. *Remote Sens.* **2024**, *16*, 290. https://doi.org/10.3390/rs16020290

Academic Editor: Salah Bourennane

Received: 17 October 2023
Revised: 7 January 2024
Accepted: 9 January 2024
Published: 11 January 2024

1. Introduction

Aquatic ecosystems play a key role in global biogeochemical cycles, biodiversity conservation, and human life [1,2]. In addition, marine resources constitute a crucial value for the tourism industry and in the production of renewable 'blue energy' from wind, wave, thermal, and biomass resources [3]. In recent decades, the effects of human-induced climate change and other anthropogenic stressors are directly and indirectly impacting these valuable ecosystems, and their resilience to these environmental disturbances remains poorly understood [2,4,5]. Effectively managing marine and coastal ecosystems to maximize socio-economic benefits and to safeguard the future effects of climate change requires comprehensive monitoring to understand their evolution and change over space and time. Since 1978, satellite remote sensing has been used as a tool for the integrated observation of aquatic systems on large scales, providing valuable information on the understanding of changing ocean dynamics at a variety of spatial, spectral, and temporal resolutions [6,7]. More recently, unmanned aerial vehicles (UAVs), also known as drones, have emerged as an intermediate monitoring platform between satellite imagery and ground-based sampling for observing coastal and marine processes at the highest spatial resolution to date. UAVs

acquire data with fine spatial resolution in near real time, achieving a higher temporal resolution than satellites by flying without the influence of cloud coverage or atmospheric effects [8,9]. UAVs can also be deployed on demand, allowing for a time-efficient, repeatable, and flexible data collection. UAVs can also be a less invasive tool than traditional field monitoring techniques [10–12] and can be used for multiple research purposes due to the variety of high-resolution sensors that can be mounted (thermal, optical RGB, multispectral, hyperspectral, or light detection and ranging, LiDAR). In addition, UAV high-resolution data can be used for satellite validation purposes by providing measurements that could reduce in situ observational efforts [8,13].

UAV-based land monitoring has been feasible with standard Structure from Motion (S*f*M) photogrammetry techniques, which finds common points between subsequent overlapped captures through triangulation and stitches them into a final georeferenced orthomosaic [14,15]. However, this technique is challenging to use in aquatic regions since water surfaces are optically dynamic, and it is not possible to identify common features between the consecutive UAV captures, thus invalidating the traditional bundle block adjustment (BBA) method in image reconstruction [13,16–18]. For this reason, most UAV-based marine studies are restricted to the coastline [12,19,20] or to small water bodies [21], where the influence of terrestrial areas provides common features to overcome the limitations of this technology in the immediately adjacent water portion. Another challenge is the reflective behavior of the water surface; UAV imagery can be significantly impacted by sun glint and surface-reflected light [8,22]. Consequently, highly reflective bright patches can appear in single captures and in the final orthomosaic even with photogrammetric processing techniques [13]. These limitations have significantly hindered the advancement of high-resolution studies relying on the remote observation of the marine ecosystem, highlighting the necessity of developing a tool that enables the integration and application of increasingly advanced sensors designed for UAV imagery over water surfaces.

Several techniques have been developed to georeference and mosaic aerial imagery collected over water surfaces [8,9,22–24]. De Keukelaere et al. (2023) achieved high-quality georeferenced orthomosaics through the application of the commercial VITO MapEO water software, which allowed the generation of final water quality orthomosaics (chlorophyll-a and turbidity concentration) with a spatial resolution of 2 m/px [8]. Essel et al. (2023) suggested that although direct georeferencing is the only practical solution for reconstructing orthomosaics in water-covered areas, combining it with other techniques such as BBA or Integrated Sensor Orientation (ISO) could provide an improved output that integrates the best characteristics of all these techniques [17]. However, this approach has only been validated in UAV flights that include part of the coastline, so that identifiable terrain features can serve as reference points for propagating the corrections from BBA and ISO to the rest of the captures over water. Windle and Silsbe (2021) addressed the challenges of sun glint and surface-reflected light by applying four different methods to estimate and remove this signal from UAV captures to derive more accurate remote sensing reflectance (R_{rs}) values. R_{rs} was used to estimate chlorophyll-a and the total suspended solids concentrations, which were georeferenced and mapped at each study location [9]. Román et al. (2023) updated the georeferencing and mosaicking technique in Windle and Silsbe (2021) in a case study at Maltese coastal waters by including an additional workflow to merge captures into a final centimeter-scale spatial resolution orthomosaic based exclusively on the sensor's metadata [13]. Finally, Gao et al. (2023) presented a workflow using a parametric geocoding technique for accurate georeferencing, based on geometric postulates, and it involved comparing the proportions of ground objects captured by UAVs with the corresponding image scale after conversion [25]. Much of the existing literature demonstrates the potential workflows; however, many of these approaches fail to project the correct geometry of each individual capture and obtain an accurate mosaicking workflow over aquatic regions.

In this study, an open-source technique is presented to georeference, mosaic, and map fully water-covered areas using optical RGB, thermal, and multispectral UAV data. This study includes various case studies, distributed across different locations such as Lake Erie

(Michigan, USA), the Antarctic Whalers and Fumarole Bays (Deception Island, Antarctica), and Southern Spain, specifically the San Pedro River creek (Bay of Cádiz Natural Park), the Mediterranean coast of Estepona (Málaga), and the Guadalquivir River (Doñana National Park, Cádiz). These datasets represent ecologically important habitats where UAV remote sensing can assist with marine macrophytes monitoring, thermal fumaroles detection, water quality assessment, among others. However, the focus for this paper is primarily on engineering advances in UAV image georeferencing and mosaicking rather than ecology. For this reason, although the methodology is designed to be applied to UAV flights over open seas or large water bodies, some coastal areas with mostly terrestrial features have been selected as reference points to validate the georeferencing accuracy of the method. The integration of this technique with emerging methods to remove surface-reflected light and sun glint will result in reliable final orthomosaics, representing a significant advancement in the study of marine and coastal processes.

2. Materials and Methods

2.1. Study Locations

UAV surveys were conducted at various locations in Southern Spain, Lake Erie (Michigan, USA), and the Antarctic Whalers and Fumarole Bays (Deception Island, Antarctica).

- The San Pedro River creek (Southern Spain, Figure 1a) is a shallow tidal inlet located in the southeastern corner of the outer Bay of Cádiz (36°31′45.48″N; 6°15′28.12″W). The creek is immersed in a considerable salt marsh area that still surrounds it, although anthropogenic activities have isolated it from the San Pedro River. The mouth is limited by a sandbar that has been shifting eastward from the coastline due to sediment inputs associated with the establishment of backflow weirs in the vicinity of the Cádiz Bay [26].
- Estepona urban beach (36°25′29″N; 5°8′41″W, Southern Spain, Figure 1a) has its seabed covered by extensive meadows of *Posidonia oceanica*, although in certain areas, these meadows are fragmented into small patches and are also in decline due to the presence of toxic waste, sewage, or trawling activities [27]. In addition, the last EU Non-Native Species Risk Analysis [28] documented the presence of the invasive alga species *Rugulopteryx okamurae* in the ZEC Seabed of the Bay of Estepona (ES6170036).
- The Guadalquivir River (36°52′14.70″N; 6°10′33.10″W, Southern Spain, Figure 1a) constitutes a navigable estuary stretching approximately 110 km from its mouth in the Gulf of Cádiz to the city of Sevilla, covering an area of around 1800 km^2. It flows through the Doñana National Park, which is considered a UNESCO World Heritage site [29]. Satellite images show the turbidity that characterizes its waters, and at its mouth, large chlorophyll plumes often form due to the river's discharge [30].
- Lake Erie (Figure 1b) constitutes the shallowest of the Great Lakes and is surrounded by Canada and the states of New York, Pennsylvania, Michigan, and Ohio in the U.S. [31]. The UAV survey was conducted over the Western Lake Erie Basin, from Michigan (41°49′45.66″N; 83°24′34.12″W). In recent years, the lake has been severely affected by excessive harmful algal blooms (HABs), eutrophication, and an overgrowth of cyanobacteria and diatoms [32,33].
- Whalers (62°58′38.75″S; 60°33′48.09″W) and Fumarole (62°57′58″S; 60°42′00″W) Bays are located on Deception Island (South Shetland Islands, Antarctica, Figure 1c). The presence of fumaroles and hydrothermal vents indicates the volcanic activity of the island, reaching temperatures exceeding 110 °C in some locations within these bays [34]. In fact, this remote island has experienced six major volcanic eruptions documented between 1841 and 1971 [35], shaping the island's distinctive rugged terrain, characterized by volcanic slopes or ash-covered glaciers [36].

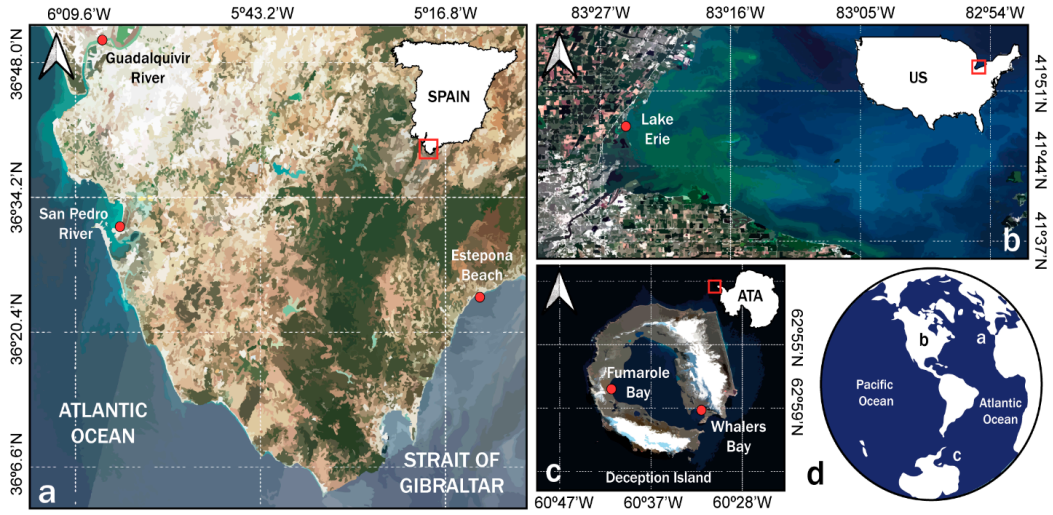

Figure 1. Tested Study Locations. (**a**) Location of the areas where UAV surveys were conducted in Southern Spain. (**b**) Location of the Lake Erie area where the UAV survey took place. (**c**) Location of the two bays where aerial thermography was carried out using UAVs on Deception Island (South Shetland Islands, Antarctica). (**d**) Global location of (**a**) Spain, (**b**) the United States (U.S.), and (**c**) Antarctica (ATA).

2.2. Data Collection

In this study, three different UAVs were used for data acquisition, equipped with different sensors:

- The quadcopter DJI Matrice 300 (M300) is equipped with both the MicaSense RedEdge-MX dual multispectral sensor and the DJI Zenmuse H20T sensor. The multispectral sensor has ten bands that capture information from the visible to near-infrared (NIR) range, with wavelengths centered, respectively, at the blue (444 and 475 nm), green (531 and 560 nm), red (650 and 668 nm), red edge (705, 717 and 740 nm), and NIR (842 nm) regions. In addition, it includes a Downwelling Light Sensor (DLS2) to account for changes in solar angle and illumination during flight. A calibration panel (RP04-1924106-0B) was used before each UAV flight for radiometric calibration. The DJI Zenmuse H20T sensor includes a 20-megapixel (MP) optical RGB Zoom sensor with a complementary metal oxide semiconductor (CMOS) 1/2.7″, a 12 MP optical RGB wide angle sensor with a CMOS 1/2.3″, and an Uncooled VOx Microbolometer thermal sensor with a focal length of 13.5 mm, capturing 640 × 512 pixel image resolution. The M300 has on-board real-time kinematic (RTK) technology to enhance georeferencing accuracy, achieving 1 cm ± 1 ppm (horizontal) and 1.5 cm ± 1 ppm (vertical) accuracies when RTK is enabled and fixed.
- The DJI Phantom 4 Pro (P4P) is equipped with the MicaSense RedEdge-MX sensor, including five bands on the electromagnetic spectrum, namely, in the blue (475 nm), green (560 nm), red (668 nm), red edge (717 nm), and NIR (842 nm) regions. This sensor also includes the DLS and is mounted using a 10° 3D-printed mount, resulting in a direct nadir viewing angle while in flight. The P4P does not have RTK technology on board, so the vertical and horizontal georeferencing accuracies are ±0.1 m and ±0.3 m (with vision positioning) and ±0.5 m and ±1.5 m (with GPS positioning), respectively.
- The DJI Mavic 2 Enterprise Advanced (M2EA) is equipped with an extra RTK module to ensure accurate georeferencing. It features a 48 MP, 1/2″ CMOS optical RGB sensor and a 640 × 512 px Uncooled VOx Microbolometer thermal sensor. This RTK quadcopter achieves a horizontal accuracy of 1 cm ± 1 ppm and a vertical accuracy of 1.5 cm ± 1 ppm, without the requirement of ground control points (GCPs).

Data acquisition was attempted to be carried out during spring tide and clear sky weather conditions. In the vast majority of study areas, this was possible except in the

Antarctic locations where cloudiness and wind conditions prevailed during the sampling days. In the flights conducted over the San Pedro River and Estepona, strong winds also hindered the execution of the intended UAV surveys. Flight missions were planned using the Universal Ground Control System (UgCS) client mission planning software (SPH Engineering, Riga, Latvia, v.4.2.156) and Pix4D Capture Pro software (Pix4D SA, Lausanne, Switzerland, v.4.12), taking into account different overlapping settings, altitudes, and flight orientations, which are displayed in Table 1 along with the dates of UAV survey execution. To support RTK measurements and improve georeferencing accuracies, a Reach RS2+ RTK GNSS antenna (EMLID) was set as the base station for all UAV surveys. Spanish (Spanish Agency for Aviation Safety, AESA), European (European Agency for Aviation Safety, EASA), and U.S. (Federal Aviation Administration, FAA) civil aviation regulations were followed during all UAV operations.

Table 1. Flight Mission Planning. Information regarding UAV flight altitude, orientation, number of flights, flight orientation angle, and dates for each study location.

	Date	# Flights	Flight Altitude	Overlapping	Flight Angle
San Pedro River (Cádiz)	21 June 2023	5	120 m	80–70%	272/92°
San Pedro River (Cádiz)	24 July 2023	2	120 m	30–10%	272/92°
Estepona (Málaga)	28 January 2023	2	100 m	80–70%	160/340°
Guadalquivir River (Cádiz)	22 March 2023	1	100 m	30–10%	240/60°
Whalers Bay (Deception Island, Antarctica)	30 January 2022	2	50 m	80–70%	225/45°
Fumarole Bay (Deception Island, Antarctica)	1 February 2022	6	50 m	80–70%	240/60°
Lake Erie (US)	17 August 2022	1	87 m	80–70%	250/70°

2.3. Data Preparation

2.3.1. Multispectral Data Collection: MicaSense RedEdge-MX Sensors

Prior to the mosaicking process, each capture taken with the multispectral sensor needs to undergo preprocessing to calculate remote sensing reflectance (R_{rs}) from the RAW data format retrieved from the UAV. Although MicaSense provides a workflow for conducting a complete radiometric calibration [37], an adaptation of DroneWQ package [9,22] was selected for this study because it is specifically designed to analyze multispectral data acquired by MicaSense sensors with a focus on aquatic regions. An adjusted version of the method was applied to accommodate the 10-band dual sensor, as the original design was tailored for MicaSense's 5-band red camera. Further information can be found in Windle and Silsbe (2021) [9].

2.3.2. Thermal Data Collection: DJI Zenmuse H20T and DJI M2EA Thermal Cameras

The thermal captures obtained using the DJI Zenmuse H20T thermal sensor and the DJI M2EA thermal sensor are converted to high-precision radiometric TIFF format using the ATygeo Thermal software (ATyges Store, Málaga, Spain, v.2.0). Only the humidity, emissivity, reflection angle, and flight height in meters need to be configured as parameters. Once the software is applied, the radiometric captures can be merged with the mosaicking code. The presence of significant thermal anomalies in the captures, such as fumaroles in Antarctic datasets, causes significant contrasts in the relative temperature values between different UAV captures. As a result, the final orthomosaic may retain artifacts in certain regions. Therefore, using the ATygeo Thermal software, it ensures that the final product maintains consistent relative temperature values in the final orthomosaic.

2.4. Data Processing: Georeferencing and Mosaicking Code

The UAV-based mosaicking code that was published in Román et al. (2023) [13] has been improved and updated in this study with reference to the previous version, so that not only the georeference of the central point of each capture is considered, but also

the geometry of each of the corners is calculated for their correct positioning in the final orthomosaic (Figure 2). The proposed algorithm has been implemented using the Python programming language, and it is publicly available at (https://github.com/SeadroneICMAN/MosaicSeadron (accessed on 10 January 2024)). In the absence of common features between UAV captures over water surfaces, this new code uses the aircraft positioning during flight (latitude, longitude, altitude, and flight orientation) and the characteristics of the sensor mounted on it (focal length, capture size, sensor size, focal plane dimensions). This code is easy-to-use and requires only the individual captures (after data preparation) as the input dataset, with the input parameters being extracted from the sensor's metadata of each capture. To facilitate the operation and understanding of the code, it has been divided into three sections: georeferencing, merging, and filtering.

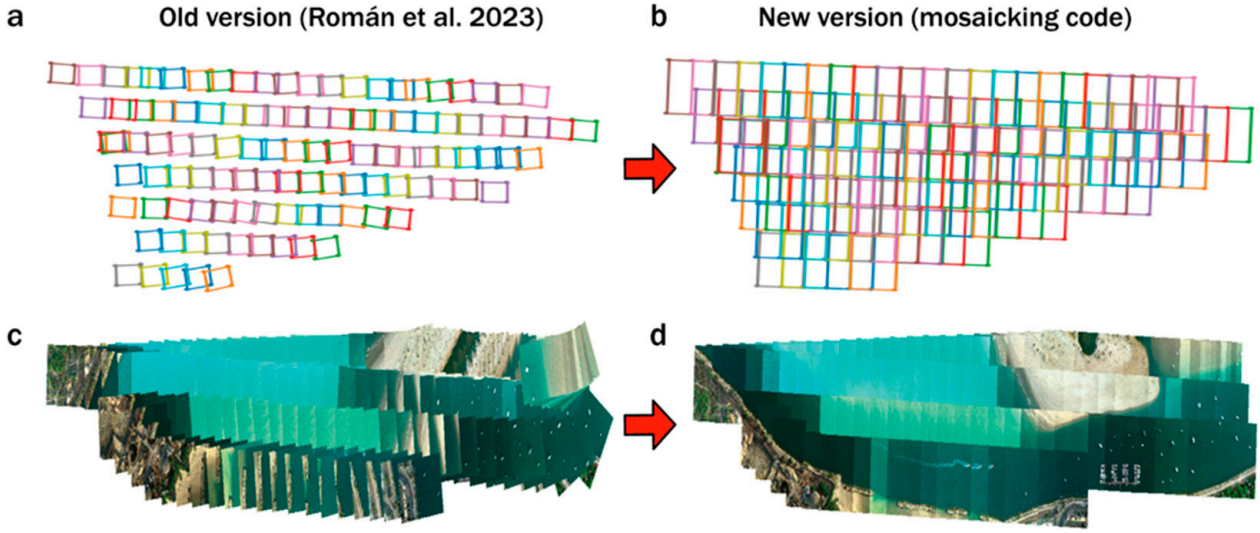

Figure 2. Improvement of the method with respect to the reference [13]. Panels (**a**,**b**) systematically represent how the new version of the code corrects the georeferencing errors from the previous version, considering the sensor size and flight angle orientation correctly. Panels (**c**,**d**) visually demonstrate how, with the new version of the code, the visual elements of the area of interest that have been mosaicked can be correctly identified.

2.4.1. Georeferencing

In this part of the code, GPS coordinates were accurately set for each individual UAV capture mainly using two main Python libraries: '*CameraTransform*' [38] and '*rasterio*' [39].

- '*CameraTransform*' generates a virtual model of the sensor using input parameters, which may vary depending on each sensor's specifications. Table 2 summarizes the parameters used in this study. It is important to note that the flight angle needs to be reduced by 90°, as it corresponds to North during the flight, whereas in '*CameraTransform*', the North is set at 0°.

The '*setGPSpos(lat, lon, alt)*' method is used to provide real latitude, longitude, and altitude coordinates for each individual capture to center it in the image centroid. Once centered, the '*gpsFromImage([row_index, column_index]*' method is applied to retrieve the latitude and longitude of each capture corner ([0, 0], [0, width −1], [height −1, 0], [height −1, width −1]). These corners allow to generate four control points to improve georeferencing accuracy.

- '*rasterio*' is used to generate a transformation matrix that indicates the latitude, longitude, and altitude (x, y, z, respectively) corresponding to each pixel (row, column) inside each UAV capture. To achieve this, four control points are generated by using the corner information retrieved in the previous step with the '*rasterio.control.GroundControlPoint(row, col, x, y, z)*' method. For example, '*rasterio.control.GroundControlPoint(0, 0, 10, 0, 0)*' means

that the pixel (0,0) of a certain capture is found in the point at 0° latitude, 10° longitude, and 0 m altitude.

Table 2. Input parameters employed in this study for the georeferencing process.

	MicaSense RedEdge-Mx	**Zenmuse H20T (RGB)**	**Zenmuse H20T (Thermal)**	**Mavic 2 Enterprise Advanced**
Focal Length (mm)	4.50	5.46	13.50	13.50
Sensor Size X (px/mm)	4.40	4.80	6.25	10.00
Sensor Size Y (px/mm)	3.30	3.60	50.00	8.00
'elevation_m'	UAV capture	UAV capture	UAV capture	UAV capture
'tilt_deg'	0	0	0	0
'roll_deg'	0	0	0	0
'heading_deg'	Flight Orientation Angle	Flight Orientation Angle	Flight Orientation Angle	Flight Orientation Angle

Once the four control points for each individual capture are set, the method '*rasterio.transform.from_gcps([gcp1, gcp2, gcp3, gcp4])*' is used to generate the transformation matrix. This matrix can be defined using the following equation (Equation (1)):

$$\begin{bmatrix} a & b & c \\ d & e & f \\ g & h & i \end{bmatrix} \; where\; c = lon_0 \; and \; f = lat_0 \tag{1}$$

Lat_0 and Lon_0 are the latitude and longitude of the (0, 0) element of a certain capture. It is important to emphasize that each matrix has a different transformation. To calculate each pixel coordinate, the '*rasterio.io.DatasetReader.xy(row, col)*' method employs a matrix product (Equation (2)) when opening each individual capture without the need for manual programming:

$$\begin{bmatrix} lon \\ lat \\ alt \end{bmatrix} = \begin{bmatrix} a & b & c \\ d & e & f \\ g & h & i \end{bmatrix} \begin{bmatrix} row \\ col \\ 1 \end{bmatrix} \tag{2}$$

2.4.2. Merging

The mosaicking code published in Román et al. (2023) [13] made use of the '*rasterio.merge.merge*' function to connect UAV captures. Although it worked well, certain limitations led to the implementation of a new merging method. This method makes use of '*rasterio*' [39] and '*numpy*' [40] libraries. '*rasterio*' is used to open each UAV capture and edit data, while '*numpy*' is used to generate the final matrix and for reading and writing operations.

The merging function is defined as 'merge(raster_paths: List[str], out_name: str, method: str = 'mean', dtype: dtype = np.float32, band_names: List[str] | None = None, **kwargs) -> str', where 'raster_paths' is the list with the absolute paths of each capture to join; 'out_name' indicates the file name containing the orthomosaic; 'method' that could be one of the four proposed merging methods, 'first' (the first written value thrives), 'min' (select the minimum pixel value), 'max' (select the maximum pixel value), or 'mean' (it calculates the average value between all coinciding pixels); and 'dtype' that is the type of data of the final matrix.

2.4.3. Filtering

Due to the positioning error that can occur in the processing of input parameters, georeferencing at centimeter resolution can have deviations of a few centimeters, that could result in duplicated features in the final orthomosaic. To address this issue and reduce the final file size, a downsampling filter is applied using the '*rasterio*' library [39] with the '*average*', '*bilinear*', or '*cubic*' techniques. As a scaling factor, the resolution is divided by 15 in

pixel width and height, although this value may vary between 15, 30, and 50, depending on the study objectives and the sensor's resolution.

2.5. Accuracy Assessment and Validation

To assess the accuracy of the georeferencing method used for mosaicking the UAV captures, the coordinates of up to 20 easily recognizable control points were taken from 25 cm/px aircraft orthophotos obtained from the Institute of Statistics and Cartography of Andalusia (IECA) website [41] for the Southern Spain datasets. In the case of flights outside of Spain, or where it has not been possible to obtain orthophotos, the orthomosaic obtained by photogrammetry (Pix4D Mapper Software, Lausanne, Switzerland, v.4.8.3) of the land area adjacent to the water-covered regions has been used as a reference. It is important to note that this method has been specifically developed for use on water-covered surfaces, as reflected in the flight plans established for each case study. Consequently, the terrestrial mosaic used as a reference for validating the georeferencing method typically coincides with the edges of the orthomosaic in a way that the selected control points may be concentrated in the same location, potentially leading to a non-representative value of the actual accuracy of the final product. The X and Y coordinates were measured for each control point on the georeferenced orthomosaic, and the difference between the known and measured coordinates yields the error for each point. The mean error was obtained by taking the arithmetic mean of the errors (Equation (3)). In addition, the Root Mean Square Error (RMSE) was calculated as an additional measure of the accuracy of the georeferencing, following Equation (4).

$$std.\,dev. = \sqrt{\left[\sum \frac{(y-\hat{y})^2}{(n-1)}\right]} \tag{3}$$

$$RMSE = \sqrt{\left[\sum \frac{(y-\hat{y})^2}{n}\right]} \tag{4}$$

Here, n represents the sample size, $\hat{y}$ represents the data considered as a reference value (orthophotos or SfM photogrammetric orthomosaics), and y represents the data being validated (mosaicked data). On the other hand, this accuracy assessment method was not feasible for the multispectral orthomosaic at Lake Erie since the UAV flight was conducted over a completely covered water area where no control points could be selected. However, similar positioning accuracy values were expected when compared to the MicaSense dual multispectral camera.

2.6. Summary

Figure 3 depicts a flowchart that summarizes the processing workflow described above for generating UAV orthomosaics over aquatic and coastal environments. The entire methodology was implemented using the Python programming language. However, QGIS (QGIS Development Team, v.3.16.14) software was chosen for the visualization and generation of the final products. The projected coordinate system used in this study was WGS84, UTM zone 29N (EPSG: 32629).

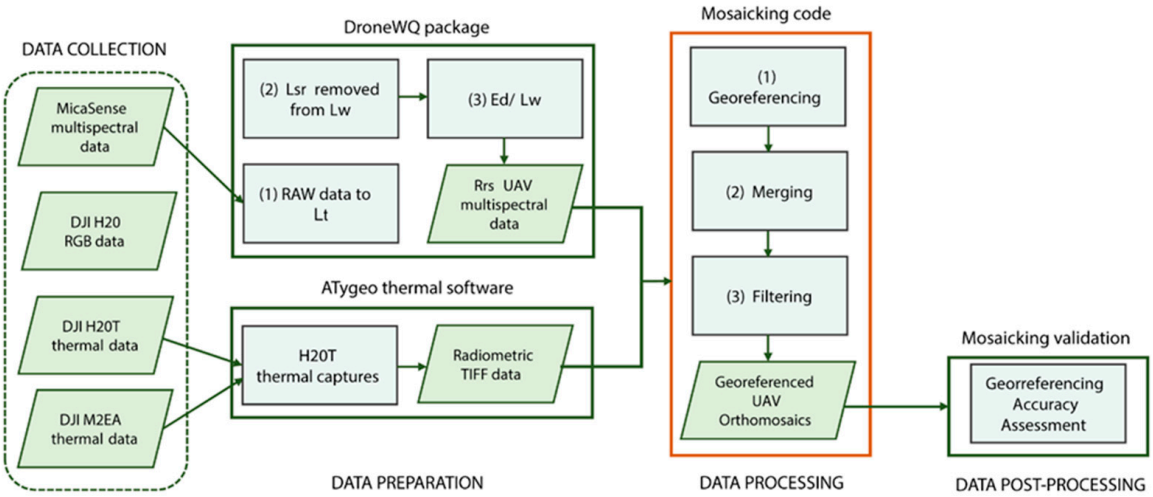

Figure 3. Flowchart summarizing the entire processing workflow followed in this study from data collection to the application of the new Python-based mosaicking code. Numbers represent the order of each processing step as indicated in the Material and Methods section. L_t: total radiance; L_{SR}: surface-reflected light; L_w: water-leaving radiance; E_d: downwelling irradiance; and R_{rs}: remote sensing reflectance.

3. Results

3.1. Optical RGB Sensor

Two different study locations, Estepona and the San Pedro River creek, were selected to show the results of applying the mosaicking code to RGB datasets acquired with the DJI H20T sensor (Figure 4). When compared to the SfM photogrammetry orthomosaic, the covered area significantly increased from 13.45 to 33 hectares for Estepona (Figure 4a) and from 1.4 to 18 hectares for the San Pedro River creek (Figure 4b), as the mosaicking technique considered the entire water area surveyed with the UAV. In fact, photogrammetry was unable to mosaic any of the water surface in the case study of the San Pedro River creek (Panel a), leading to the loss of approximately 86% of the original UAV captures. Nonetheless, photogrammetry was able to generate an orthomosaic up to an approximate depth of 4 m (approximately 200 m from the waterline) in clearer waters such as the Estepona case study (Panel b), although with the mosaicking technique, the covered distance from the coastline increased to 545 m, recovering 61% of the lost information at any depth from the original UAV captures.

When compared to fixed ground control points, this new method achieved a standard deviation and RMSE of 2.88 m and 8.71 m for the San Pedro River flight, and 3.68 m and 8.25 m for the Estepona flight in georeferencing accuracy, respectively. Consequently, minor visual artifacts appeared in the final orthomosaic as a result of a georeferencing error that was carried over into the merging processing step, although they are not significant for marine/coastal applications. Georeferencing accuracy statistics remained relatively consistent around the mean when examining the UAV's orientation angle in relation to true North during flight (See Supplementary Material Figure S1), exhibiting marginal fluctuations with changes in flight orientation. In fact, the disparity between the highest and lowest standard deviation was 0.31 m, and the variation in RMSE amounted to 1.79 m.

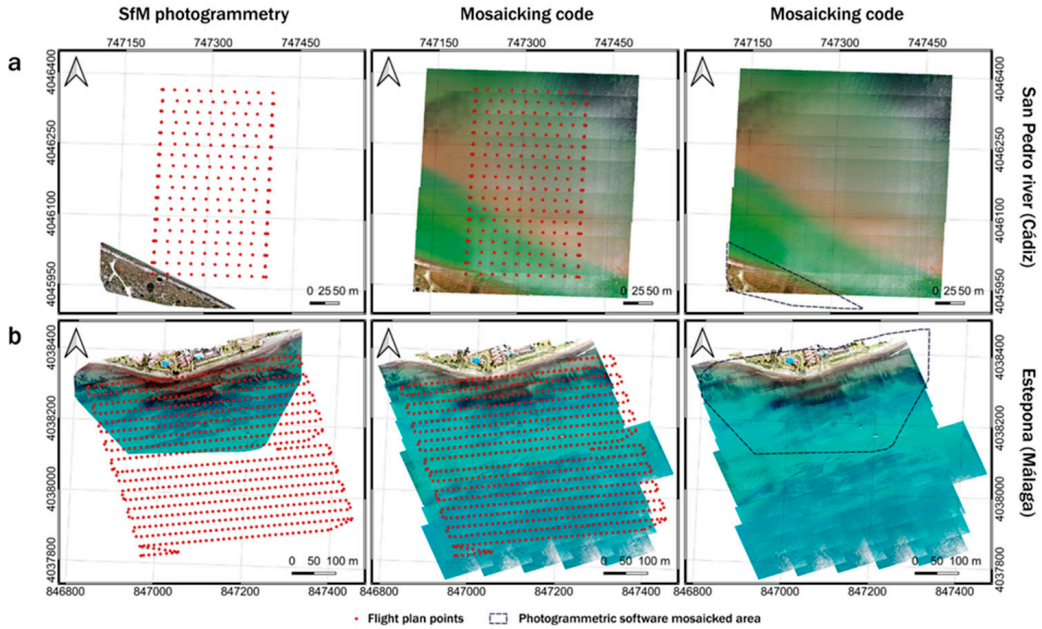

Figure 4. Application of the mosaicking technique to optical RGB datasets. Comparison between the georeferenced orthomosaic generated after an SfM photogrammetry process and the georeferenced orthomosaic generated after applying the Python-based mosaicking code in (**a**) the San Pedro River creek case study and (**b**) the Estepona case study. Red dots indicate each flight plan points, and the black dashed lines frame the mosaicked area using the SfM photogrammetry process.

3.2. Thermal Sensor

To demonstrate the adaptability and applicability of the mosaicking code to data collected with thermal sensors, a pair of Antarctic datasets (Whalers Bay and Fumarole Bay) captured using the DJI Mavic 2 Enterprise Advanced (M2EA) thermal sensor have been selected. These locations were chosen due to the high volcanic and geothermal activity on Deception Island, so that the detection of these fumaroles along the coastline can provide valuable and essential information for volcanic activity warning systems on the island, extending now to coastal areas and into the water. In Figure 5, both locations are displayed as orthomosaics, differentiating between the original thermal captures and the thermal captures pre-processed with the ATygeo Thermal software into relative temperature values (°C). In the zoomed areas, this result highlights the need to transform the thermal captures to calibrate the thermal sensor temperature values, as thermal anomalies are detected with higher clarity and level of detail.

Although the results show a higher precision in the merging of the captures due to the lower spatial resolution of the thermal sensor, minor visual artifacts still appear as a result of the georeferencing error that accumulates between captures. This error is further amplified in this study, as seen in the specific areas highlighted in Figure 5b–f, because the flights were conducted with the maximum possible overlap. In any case, the method achieved good accuracy values for georeferencing, especially when focusing on its primary application purpose in water-covered areas, with a standard deviation and RMSE of 2.51 m and 4.52 m for the Fumarole Bay flight, and 2.98 m and 5.86 m for the Whalers Bay flight, respectively. Furthermore, similar to optical RGB imagery, a significant amount of lost information by mosaicking with photogrammetric software was successfully recovered with this mosaicking technique, reaching 59% for the Fumarole Bay flight and 69% for the Whalers Bay flight.

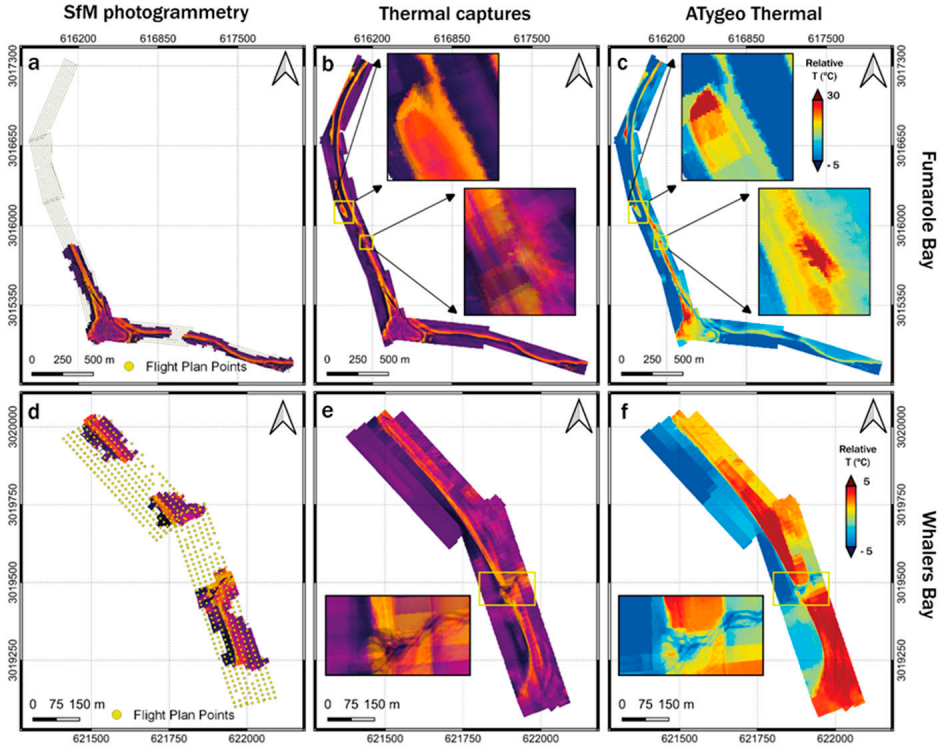

Figure 5. Application of the mosaicking technique to thermal datasets. Comparison between the performance of (**a**,**d**) SfM photogrammetry, (**b**,**e**) the mosaicking code on the original thermal captures taken by the M2EA, and (**c**,**f**) the thermal captures corrected with ATygeo Thermal software, using two datasets captured on Deception Island (Antarctica). Both datasets exhibit temperature oversaturation, particularly above the maximum values displayed on the color bar. Yellow dots indicate each flight plan points. Specific areas showing the presence of thermal anomalies in Fumarole Bay and a coastal stream in Whalers Bay have been outlined.

3.3. Multispectral Sensor

The mosaicking method was also successfully applied to multispectral UAV captures that were collected for water quality assessment. Figure 6 shows a graphical matrix illustrating the main configurations and issues that affected the appearance of an orthomosaic created from water captures. First, an incorrect orientation angle configuration as observed in the Guadalquivir River dataset (Figure 6a), with contrasting UAV heading orientations (South East–North West) resulted in clearly identifiable striping in the final orthomosaic (Figure 6b,c). Secondly, an excessive overlap configuration led to an increased number of visual artifacts in the final orthomosaic (Figure 6e), which can be reduced by setting less overlap between captures. In addition, planning efficiency is higher when no overlap is considered since the area is covered in the same time interval with a lower number of batteries and flight time. For example, in this case study of the San Pedro River (Figure 6d), two flights with 30% overlap between captures covered a total of 68 hectares, while five flights were required to cover almost the same area with 80% frontal and lateral overlap (Figure 6e,f). Finally, the influence of specular sun glint, when direct sunlight reflects off a wave facet or surface, must be considered for the viewing angle of the sensor. When ignored, the white patches of specular sun glint are noticeable, as seen in the final orthomosaic for the Lake Erie case study (Figure 6g–i). In this case, the filtering procedure described in Windle and Silsbe (2022) [9] is applied to individual captures to eliminate the specular sun glint, resulting in a much cleaner final mosaic (Figure 6h).

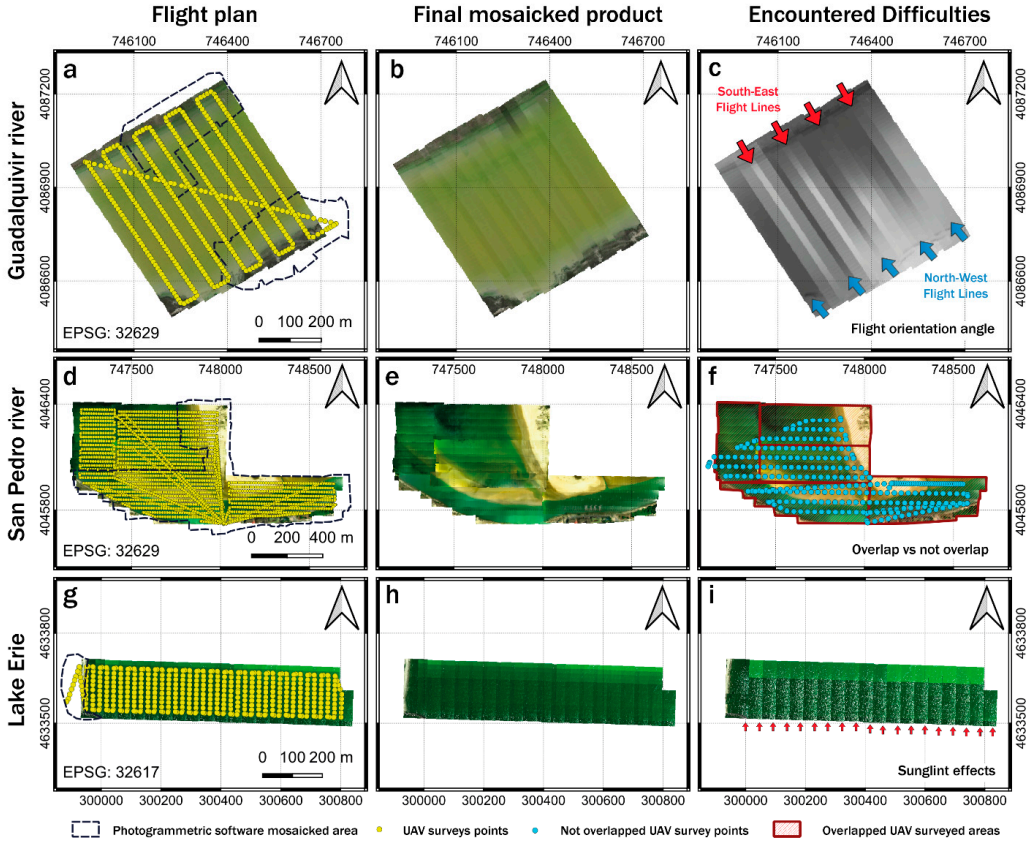

Figure 6. Encountered difficulties in mosaicking multispectral imagery. Guadalquivir River case study: (**a**) flight plan (yellow dots) and the area covered by photogrammetry (delimited by black lines); (**b**) final mosaicked product without flight trajectory angle correction; and (**c**) issue with flight orientation angle. San Pedro River case study: (**d**) flight plan (yellow dots) and the area covered by photogrammetry (delimited by black lines); (**e**) final mosaicked product considering 80% frontal and side overlapping; and (**f**) comparison of the covered area with and without considering overlap. Blue dots indicate the covered area when not considering overlap in the flight plan, while red rectangles represent the covered area when considering overlap in each flight plan. Lake Erie case study: (**g**) flight plan (yellow dots) and area covered by photogrammetry (delimited by black lines); (**h**) final mosaicked product after applying sun glint correction; and (**i**) issue of sun glint effects on the final mosaicked product.

In all multispectral study locations, despite encountering difficulties that impacted the final product's appearance, the water coverage is greater with the new mosaicking method than when mosaicked with photogrammetry. Furthermore, this approach could be applied directly to merge UAV captures directly after employing water quality retrieval algorithms, to generate a final map displaying scientifically valuable information for addressing fine-scale marine phenomena. Accuracy assessment was conducted on the San Pedro River and Guadalquivir River datasets, as it was possible to use some terrestrial features mosaicked by photogrammetry as a reference. The method yielded favorable accuracy values for georeferencing, particularly with the Guadalquivir River flight, where the standard deviation and RMSE were 4.89 m and 8.70 m, respectively. However, accuracy values were not as good as expected, probably due to the absence of RTK technology and adverse weather conditions, achieving a standard deviation and RMSE of 2.56 m and 14.55 m, respectively. Lastly, accuracy statistics for georeferencing could not be computed for the Lake Erie dataset since the entire covered area was above the water surface.

4. Discussion

UAVs have shown great potential in addressing inherent challenges in optical oceanography at finer scales. Consequently, there is a need to develop an efficient, accurate, fast, and versatile tool to harness the advantages of this promising technology in aquatic environments. As aforementioned, photogrammetric techniques based on parametric georeferencing fail when reconstructing orthomosaics over water surfaces by stitching multiple images, and previous studies have highlighted direct georeferencing as the only practical alternative for mosaicking UAV captures [19]. This study presents a new direct georeferencing-based mosaicking technique, resulting in a coverage extension up to four times of that achieved by photogrammetric software at study locations, all of which are near the coastline (Figure 4). Although commercial software employing this technique has achieved spatial resolutions of up to 2 m/px for multispectral imagery [8], this study represents the most accurate open-source approach to date, reaching spatial resolutions of up to 0.5 m/px. In addition, its applicability is demonstrated for optical RGB, thermal, and multispectral imagery, expanding the range of marine and coastal studies across various spatial and temporal scales. Examples of its potential applications include fauna monitoring [42,43], marine geomorphology [44], coastal habitat mapping [45–47], water quality assessment [9,22], and as a calibration/validation tool for satellite products [8,48].

Generally, the georeferenced product obtained after the mosaicking process achieves reasonably good georeferencing statistics (a few meters would be enough to provide a high-quality orthomosaic of water surfaces), thus demonstrating its validity as a reliable reference tool for calibration and validation purposes. In fact, a clear improvement in the statistics is observed when a comparison is conducted among UAVs (RTK vs. not RTK), highlighting the fact that DJI's RTK technology provides more accurate results. Furthermore, certain UAV surveys did not achieve RMSE values as good as those obtained at other study locations. Several factors could be related to this issue, such as adverse weather conditions that affected the entire UAV survey over the Estepona beach and San Pedro River (windy weather conditions), impacting both the optical RGB and the multispectral sensor's GPS. Another potential factor is the spatial resolution of the employed sensors, as the accuracy assessment process relies on visually identifiable terrestrial features between the mosaicked products and the orthophotos used as references. In fact, although quite similar to the other sensors, the best accuracies were obtained with the thermal sensors, which provided the lowest spatial resolution among the tested sensors. Finally, most of the flights conducted in this study were over water-covered surfaces, so only identifiable points on the terrestrial regions were used as references for validation, generally coinciding with the edges of the orthomosaic (except for thermal flights, where the coverage is mostly terrestrial). At these edges, the georeferencing tends to be worse since obtaining the orthomosaic's coordinates involves the projection of the individual captures onto a horizontal plane, so the central area of the plane is more stable, and the aspect ratio remains the same regardless of the projection used. The combination of these aspects contributes to an increase in georeferencing error, although standard deviation values do not exceed 5 m for all UAV surveys, indicating that the majority of differences between the final orthomosaic and the reference fall within a relatively narrow range of values, suggesting georeferencing accuracy is well controlled and consistent.

The flight planning process takes on greater importance in the implementation of this mosaicking methodology, as there are several aspects to consider that demonstrate a marked influence on the quality of the final product, especially when dealing with multispectral imagery. Overlapping constitutes a fundamental factor when finding common features for alignment in the photogrammetry process but can produce more visual artifacts in the final orthomosaic after the merging process with this mosaicking workflow. Therefore, it is recommended to conduct flights with minimal overlap between captures while ensuring sufficient coverage to avoid any areas being left uncovered between flight lines. Furthermore, based on UAV surveys in the San Pedro River (Figure 6d–f), it has been demonstrated that flying without overlap is more efficient, as it covers almost the same

area in a much shorter time interval (five vs. two pairs of batteries). Another aspect to consider is the orientation angle of the UAV with respect to the North direction during the flight. The UAV survey in the Guadalquivir River (Figure 6a–c) shows that band stripping can occur if the UAV faces opposite direction angles in each transect flight line. Hence, it is necessary for the UAV to maintain the same flight heading orientation angle on all transects. In addition, experimental flights carried out over the San Pedro River at varying flight heading orientation angles in relation to the sun have substantiated the method's robustness. The statistical evaluations of georeferencing accuracy and the visual appearances of the final orthomosaics indicate an absence of significant differences. However, it is important to emphasize that not all flight planning software offers this option, and UgCS client mission planning software or Ground Station Pro (GSP) application are suggested as effective solutions.

While not a caveat of this mosaicking code, there are other aspects unrelated to flight planning that could also affect the quality of the final product if not adequately addressed. For multispectral imagery, Windle and Silsbe (2022) [9] suggest that the effect of wind-driving waves can lead to the appearance of sun glint and reflected skylight in individual UAV captures. The simplest way to avoid sun glint effects when working with UAV imagery is to consider flying close to solar noon and taking into account the appropriate flight direction. However, the dynamic nature of the water surface makes it challenging to completely eliminate sun glint in individual captures [49]. As a result, several methods have been successfully attempted to remove the sun glint effect. These include the approaches proposed by Muslim et al. (2019) [50] and Hochberg et al. (2003) [51], as well as the HydroLight simulations utilized by Windle and Silsbe (2021) [9]. In the case study of Lake Erie (Figure 6g–i), it is demonstrated that obtaining a much cleaner orthomosaic using this methodology is possible when sun glint is masked, since this mosaicking code calculates the mean value of coincident captures in each pixel without taking into account the masked values. However, Gray et al. (2022a) [22] highlights that the methods used for reflected skylight removal may not be practical in surveys employing long-endurance UAVs, as they assume that sky conditions and sun angles remain constant throughout the flight, which is not the case in these situations. For thermal imagery, Szostak et al. (2023) [52] and Aragón et al. (2020) [53] suggest that reducing the vignetting effect in individual thermal captures could have a positive impact on the appearance of the final result. After some preliminary tests (not included as results in this manuscript), it is concluded that, for the sensors used (DJI H20T and DJI M2EA), the final result does not show significant improvements after applying a de-vignetting correction process. This study demonstrates that the radiometric pre-processing of thermal captures captured directly by the UAV significantly improves the final orthomosaic (Figure 5), which also presents more quantifiable relative temperature values for the user.

Although this method provides an accurate approximation of the results obtained by photogrammetry in terrestrial environments, it could be improved by reducing the georeferencing errors that persist between UAV captures, resulting in visual artifacts in the final product. Essel et al. (2023) [19] suggested the combined use of BBA and ISO with direct georeferencing can yield positive results by first stitching images over common points on the coastline and subsequently propagating the obtained error to areas covered by water. This would limit the studies to the proximity of the coastline, as it cannot be applied to offshore aquatic systems due to the lack of referencing features. On the other hand, the scientific community is increasingly adopting the use of sensors onboard UAVs to carry out radiometric measurements with multispectral and hyperspectral sensors. Although there are studies that have obtained values of R_{rs} with UAV data that have been validated in situ supported by good statistical values [9,10], future research should focus on accurately addressing the inherent complexities of seawaters, such as sun glint and reflected skylight removal, maintaining appropriate viewing geometries, and constraining uncertainties on a per-sensor basis. This will lead to improvements in existing techniques for water quality monitoring, as suggested by Gray et al. (2022a) [38]. In any case, this mosaicking technique

has demonstrated its potential to mosaic full water imagery where S*f*M photogrammetry oftentimes fails, achieving acceptable precision and serving as a foundation for future research aimed at enhancing its performance and addressing its limitations.

5. Conclusions

The UAV georeferencing and mosaicking method described in this study constitutes an open-source, flexible, and easy-to-use approach that has been successfully applied to optical RGB, thermal, and multispectral imagery with centimeter-scale spatial resolution. The Python-based mosaicking algorithm (https://github.com/SeadroneICMAN/MosaicSeadron (accessed on 10 January 2024)) allows scientists to survey aquatic systems, overcoming limitations faced by photogrammetry and offers a viable alternative to traditional monitoring techniques that involve logistical and time constrains. Several flight conditions and parameterizations have been simulated to provide the best setup for addressing unexpected issues in these systems, including less overlapping between UAV captures (not more than 30% frontal and side overlap), same flight orientation with respect to the North for each flight line, and avoiding unfavorable weather conditions during flight. The presented method not only enhances current workflows but also introduces a modular, scalable solution adaptable to future algorithmic advancements that seek to refine this tool's capabilities. Its effectiveness has been validated across various coastal study sites for practical and verification reasons, showcasing the method's versatility. Although initially designed for generating high-quality orthomosaics from any aquatic surface, the technique's real-world applicability has been confirmed, establishing it as a reliable resource in aquatic research. The best case achieved a Root Mean Square Error of 4.52 m and a standard deviation of 2.51 m for georeferencing accuracy. The ocean science community needs robust approaches to understand uncertainties in marine and coastal systems, and this method represents a significant advance in the use of UAVs to address, at a finer scale, the understanding of marine ecosystems.

Supplementary Materials: The following supporting information can be downloaded at: https://www.mdpi.com/article/10.3390/rs16020290/s1; Figure S1: Testing the mosaicking code performance by varying UAV flight orientation angle. Tested angles and their complements: (A) 0°/180°; (B) 45°/225°; (C) 90°/270°; and (D) 135°/315°.

Author Contributions: The original draft of this paper was written by A.R., and it was reviewed and edited by S.H., A.E.W., A.T.-S. and G.N. The algorithm was designed by A.R. and S.H. UAV surveys were conducted by A.R., A.E.W., A.T.-S. and G.N., A.T.-S. and G.N. supervised the project. All authors have read and agreed to the published version of the manuscript.

Funding: This research has been funded by the European Union's Horizon 2020 research and innovation programme REWRITE project (grant number 101081357), PY20-00244 (SAT4ALGAE) PROJECT and TURISDRON (PROYEXCEL 00052) project by Junta de Andalucía, RTI2018-098048B-100 (PiMetAn), PID2021-1257830B-100 (DICHOSO), and EQC2018-004275-P and TED2021-129230B-I00 funded by MCIN/AEI/10.13039/501100011033 and by 'ERDF A way of making Europe'. The research that led to this publication was conducted with the support of a US–Spain Fulbright grant and of the Junta de Andalucía. A.R. is supported by grant FPU19/04557 funded by Ministry of Universities of the Spanish Government. This research has been financially supported by the agreement between the Spanish Ministry for Ecological Transition and Demographic Challenge and CSIC, funded by the European Union-Next Generation Program to contribute to the MSFD. This work represents a contribution to CSIC Thematic Interdisciplinary Platform PTI TELEDETECT.

Data Availability Statement: The mosaicking and georeferencing code is available in a GitHub repository. Its use must be acknowledged by citing this manuscript: https://github.com/SeadroneICMAN/MosaicSeadron (accessed on 10 January 2024).

Acknowledgments: The authors would like to thank the Institute of Statistics and Cartography of Andalusia (IECA) for distributing orthophotos of the study locations for validation purposes. We also thank María Nicolau, David Roque-Atienza, and Antonio Moreno from ICMAN-CSIC for their contributions in the performance of UAV surveys.

Conflicts of Interest: Author Anna E. Windle was employed by the Science Systems and Applications Inc. The remaining authors declare that the research was conducted in the absence of any commercial or financial relationships that could be construed as a potential conflict of interest.

References

1. Borges, A.V.; Abril, G.; Darchambeau, F.; Teodoru, C.R.; Deborde, J.; Vidal, L.O.; Lambert, T.; Bouillon, S. Divergent biophysical controls of aquatic CO_2 and CH_4 in the world's two largest rivers. *Sci. Rep.* **2015**, *5*, 15614. [CrossRef] [PubMed]
2. Spyrakos, E.; O'Donnell, R.; Hunter, P.D.; Miller, C.; Scott, M.; Simis, S.G.; Neil, C.; Barbosa, C.C.; Binding, C.E.; Bradt, S.; et al. Optical types of inland and coastal waters. *Limnol. Oceanogr.* **2018**, *63*, 846–870. [CrossRef]
3. Bari, A. Our Oceans and the Blue Economy: Opportunities and Challenges. *Procedia Eng.* **2017**, *194*, 5–11. [CrossRef]
4. Lovejoy, T.E.; Hannah, L. *Climate Change and Biodiversity*; CTY University Press: New Haven, CT, USA, 2005; p. 418.
5. Petrescu, A.M.R.; Lohila, A.; Tuovinen, J.P.; Baldocchi, D.D.; Desai, A.R.; Roulet, N.T.; Vesala, T.; Dolman, A.J.; Oechel, W.C.; Marcolla, B.; et al. The uncertain climate footprint of wetlands under human pressure. *Proc. Natl. Acad. Sci. USA* **2015**, *112*, 4594–4599. [CrossRef]
6. Blondeau-Patissier, D.; Gower, J.F.R.; Dekker, A.G.; Phinn, S.R.; Brando, V.E. A review of ocean color remote sensing methods and statistical techniques for the detection, mapping and analysis of phytoplankton blooms in coastal and open ocean. *Prog. Oceanogr.* **2014**, *123*, 123–144. [CrossRef]
7. McClain, C.R.; Franz, B.A.; Werdell, P.J. Genesis and Evolution of NASA's Satellite Ocean Color Program. *Front. Remote Sens.* **2022**, *3*, 938006. [CrossRef]
8. De Keukelaere, L.; Moelans, R.; Knaeps, E.; Sterckx, S.; Reusen, I.; De Munck, D.; Simis, S.G.; Constantinescu, A.M.; Scrieciu, A.; Katsouras, G.; et al. Airborne Drones for Water Quality Mapping in Inland Transitional and Coastal Waters—MapEO Water Data Processing and Validation. *Remote Sens.* **2023**, *15*, 1345. [CrossRef]
9. Windle, A.E.; Silsbe, G.M. Evaluation of Unoccupied Aircraft System (UAS) Remote Sensing Reflectance Retrievals for Water Quality Monitoring in Coastal Waters. *Front. Environ. Sci.* **2021**, *9*, 674247. [CrossRef]
10. Cheng, K.H.; Chan, S.N.; Lee, J.H.W. Remote sensing of coastal algal blooms using unmanned aerial vehicles (UAVs). *Mar. Pollut. Bull.* **2020**, *152*, 110889. [CrossRef] [PubMed]
11. Koparan, C.; Koc, A.B.; Privette, C.V.; Sawyer, C.B. In Situ Water Quality Measurements Using and Unmanned Aerial Vehicle (UAV) System. *Water* **2018**, *10*, 264. [CrossRef]
12. Ying, H.; Xia, K.; Huang, X.; Feng, H.; Yang, Y.; Du, X.; Huang, L. Evaluation of water quality based on UAV images and the IMP-MPP algorithm. *Ecol. Inform.* **2021**, *61*, 101239. [CrossRef]
13. Román, A.; Tovar-Sánchez, A.; Gauci, A.; Deidun, A.; Caballero, I.; Colica, E.; D'Amico, S.; Navarro, G. Water-Quality Monitoring with a UAV-Mounted Multispectral Camera in Coastal Waters. *Remote Sens.* **2023**, *15*, 237. [CrossRef]
14. Snavely, N. Scene Reconstruction and Visualization from Internet Photo Collections. Unpublished. Ph.D. Thesis, University of Washington, Washington, DC, USA, 2008.
15. Westoby, M.; Brasington, J.; Glasser, N.F.; Hambrey, M.J.; Reynolds, J.M. 'Structure-from-Motion' photogrammetry: A low-cost, effective tool for geoscience applications. *Geomorphology* **2012**, *179*, 300–314. [CrossRef]
16. Essel, B.; McDonald, J.; Bolger, M.; Cahalane, C. Initial Study Assessing the Suitability of Drones with Low-Cost GNSS and IMU for Mapping over Featureless Terrain Using Direct Georeferencing. In Proceedings of the International Archives of Photogrammetry, Remote Sensing and Spatial Information Sciences, Volume XLIII-B2-2022, XXIV ISPRS Congress (2022 edition), Nice, France, 6–11 June 2022. [CrossRef]
17. Essel, B.; Bolger, M.; McDonald, J.; Cahalane, C. Developing a Theoretical Assessment Method for an Assisted Direct Georeferencing Approach to Improve Accuracy when Mapping over Water: The Concept, Potential and Limitations. In Proceedings of the ISPRS 12th International Symposium on Mobile Mapping Technology (MMT), Padua, Italy, 24–26 May 2023. [CrossRef]
18. Knaeps, E.; Moelans, R.; Strackx, G.; Keukelaere, L.D.; Lemey, E. *Mapping Water Quality with Drones: Test Case in Texel*; International Association of Dredgins Companies: Voorburg, The Netherlands, 2019; pp. 6–16.
19. Choo, Y.; Kang, G.; Kim, D.; Lee, S. A study on the evaluation of water-bloom using image processing. *Environ. Sci. Pollut. Res.* **2018**, *25*, 36775–36780. [CrossRef] [PubMed]
20. Johansen, K.; Dunne, A.F.; Tu, Y.; Almashharawi, S.; Jones, B.H.; McCabe, M.F. Dye tracing and concentration mapping in coastal waters using unmanned aerial vehicles. *Sci. Rep.* **2022**, *12*, 1141. [CrossRef] [PubMed]
21. Cillero-Castro, C.; Domínguez Gómez, J.A.; Delgado Martín, J.; Hinojo Sánchez, B.A.; Cereijo Arango, J.L.; Cheda Tuya, F.A.; Díaz-Varela, R. An UAV and Satellite Multispectral Data Approach to Monitor Water Quality in Small Reservoirs. *Remote Sens.* **2020**, *12*, 1514. [CrossRef]
22. Gray, P.C.; Windle, A.E.; Dale, J.; Savelyev, I.B.; Johnson, Z.I.; Silsbe, G.M.; Larsen, G.D.; Johnston, D.W. Robust ocean color from drones: Viewing geometry, sky reflection removal, uncertainty analysis, and a survey of the Gulf Stream front. *Limnol. Oceanogr. Methods* **2022**, *20*, 656–673. [CrossRef]
23. O'Shea, R.E.; Laney, S.R.; Lee, Z. Evaluation of glint correction approaches for fine-scale ocean color measurements by lightweight hyperspectral imaging spectrometers. *Appl. Opt.* **2020**, *59*, B18–B34. [CrossRef]
24. Zhang, X.; He, S.; Shabani, A.; Zhai, P.W.; Du, K. Spectral sea surface reflectance of skylight. *Opt. Express* **2017**, *25*, A1–A13. [CrossRef] [PubMed]

25. Gao, H.; Yu, Y.; Huang, X.; Song, L.; Li, L.; Li, L.; Zhang, L. Enhancing the Localization Accuracy of UAV Images under GNSS Denial Conditions. *Sensors* **2023**, *23*, 9751. [CrossRef]
26. Martínez del Pozo, J.A.; Anfuso, G.; Gracia, F.J. Recent evolution of a tidal delta in Cadiz Bay (SW Spain) due to human interventions. In Proceedings of the Fifth International Conference on the Mediterranean Coastal Environment, MEDCOAST'01, Hammamet, Tunisia, 23–27 October 2001; pp. 1425–1433.
27. Asensi, A.; Diez-Garretas, B. Coastal Vegetation. In *The Vegetation of the Iberian Peninsula*; Plant and Vegetation, 13; Loidi, J., Ed.; Springer: Cham, Switzerland, 2015. [CrossRef]
28. Altamirano, M.; Zanolla, M. EU Non-Native Organism Risk Assessment Scheme. In *EU Non-Native Species Risk Assessment Analysis—Risk Assessment Template v.1.0*; European Union: Brussels, Belgium, 2015.
29. Ruiz, J.; Polo, M.J.; Díez-Minguito, M.; Navarro, G.; Morris, E.P.; Huertas, E.; Caballero, I.; Contreras, E.; Losada, M.A. *The Guadalquivir Estuary: A Hot Spot for Environmental and Human Conflicts, Environmental Management and Governance*; Volume 8 of the Series Coastal Research Library; EBSCO: Ipswich, MA, USA, 2014; pp. 199–232. [CrossRef]
30. Caballero, I.; Navarro, G. Analisis multisensor para el estudio de los patrones de turbidez en el estuario del Guadalquivir. *Rev. Teledeteccion* **2016**, *46*, 1–17. [CrossRef]
31. Neumann, A.; Dong, F.; Shimoda, Y.; Arnillas, C.A.; Javed, A.; Yang, C.; Zamaria, S.; Mandal, S.; Wellen, C.; Paredes, D.; et al. A review of the current state of process-based and data-driven modelling: Guidelines for Lake Erie managers and watershed modellers. *Environ. Rev.* **2021**, *29*, 443–490. [CrossRef]
32. Stumpf, R.P.; Wynne, T.T.; Baker, D.B.; Fahnenstiel, G.L. Interannual variability of cyanobacterial blooms in Lake Erie. *PLoS ONE* **2012**, *7*, e42444. [CrossRef] [PubMed]
33. Watson, S.B.; Miller, C.; Arhonditsis, G.; Boyer, G.L.; Carmichael, W.; Charlton, M.N.; Confesor, R.; Depew, D.C.; Höök, T.O.; Ludsin, S.A.; et al. The re-eutrophication of Lake Erie: Harmful algal blooms and hypoxia. *Harmful Algae* **2016**, *56*, 44–66. [CrossRef]
34. Tovar-Sánchez, A.; Román, A.; Roque-Atienza, D.; Navarro, G. Applications of unmanned aerial vehicles in Antarctic environmental research. *Sci. Rep.* **2021**, *11*, 21717. [CrossRef]
35. Zandomeneghi, D.; Barclay, A.; Almendros, J.; Ibañez-Godoy, J.M.; Wilcock, W.S.D.; Ben-Zvi, T. Crustal structure of Deception Island volcano from P wave seismic tomography: Tectonic and volcanic implications. *J. Geophys. Res.* **2009**, *114*, B06310. [CrossRef]
36. Duarte, B.; Gameiro, C.; Matos, A.R.; Figueiredo, A.; Silva, M.S.; Cordeiro, C.; Caçador, I.; Reis-Santos, P.; Fonseca, V.; Cabrita, M.T. First Screening of Biocides, Persistent Organic Pollutants, Pharmaceutical and Personal Care Products in Antarctic Phytoplankton from Deception Island by FT-ICR-MS. *Chemosphere* **2021**, *274*, 129860. [CrossRef]
37. MicaSense. Image Processing Tutorials. 2022. Available online: https://github.com/micasense/imageprocessing/actions (accessed on 27 November 2022).
38. Gerum, R.C.; Richter, S.; Winterl, A.; Mark, C.; Fabry, B.; Le Bohec, C.; Zitterbart, D.P. CameraTransform: A Python package for perspective corrections and Image mapping. *SoftwareX* **2019**, *10*, 100333. [CrossRef]
39. Mapbox. Rasterio. 2015. Available online: https://rasterio.readthedocs.io/en/stable/ (accessed on 8 March 2023).
40. Harris, C.R.; Millman, K.J.; Van Der Walt, S.J.; Gommers, R.; Virtanen, P.; Cournapeau, D.; Wieser, E.; Taylor, J.; Berg, S.; Smith, N.J.; et al. Array programming with NumPy. *Nature* **2020**, *858*, 357–362. [CrossRef]
41. Institute of Statistics and Cartography of Andalusia. 2023. Available online: https://www.juntadeandalucia.es/institutodeestadisticaycartografia (accessed on 8 January 2024).
42. Gazagne, E.; Gray, R.J.; Ratajszczak, R.; Brotcorne, F.; Hambuckers, A. Unmanned aerial vehicles (UAVs) with thermal infrared (TIR) sensors are effective for monitoring and counting threatened Vietnamese primates. *Primates* **2023**, *64*, 407–413. [CrossRef]
43. Povlsen, P.; Linder, A.C.; Larsen, H.L.; Durdevic, P.; Arroyo, D.O.; Bruhn, D.; Pertoldi, C.; Pagh, S. Using Drones with Thermal Imaging to Estimate Population Counts of European Hare (*Lepus europaeus*) in Denmark. *Drones* **2023**, *7*, 5. [CrossRef]
44. Seymour, A.; Ridge, J.; Rodriguez, A.; Newton, E.; Dale, J.; Johnston, D.W. Deploying Fixed Wing Unoccupied Aerial Systems (UAS) for Coastal Morphology Assessment and Management. *J. Coast. Res.* **2017**, *34*, 704–714. [CrossRef]
45. Jiang, X.; Gao, M.; Gao, Z. A novel index to detect green-tide using UAV-based RGB imagery. *Estuar. Coast. Shelf Sci.* **2020**, *245*, 106943. [CrossRef]
46. Kellaris, A.; Gil, A.; Faria, J.; Amaral, R.; Moreu-Badia, I.; Neto, A.; Yesson, C. Usinglow-cost drones to monitor heterogeneous submerged seaweed habitats: A case study in the Azores. *Aquat. Conserv.* **2019**, *29*, 1909–1922. [CrossRef]
47. Román, A.; Tovar-Sánchez, A.; Olivé, I.; Navarro, G. Using a UAV-Mounted Multispectral Camera for the Monitoring of Marine Macrophytes. *Front. Mar. Sci.* **2021**, *8*, 722698. [CrossRef]
48. Gray, P.; Larsen, G.D.; Johnston, D.W. Drones address an observational blind spot for biological oceanography. *Front. Ecol. Environ.* **2022**, *20*, 413–421. [CrossRef]
49. Tiškus, E.; Bučas, M.; Vaičiūtė, D.; Gintauskas, J.; Babrauskienė, I. An Evaluation of Sun-Glint Correction Methods for UAV-Derived Secchi Depth Estimations in Inland Water Bodies. *Drones* **2023**, *7*, 546. [CrossRef]
50. Muslim, A.M.; Wei-Sheng, C.; Che-Din, M.S.; Khalil, I.; Hossain, M. Coral Reef Mapping of UAV: A Comparison of Sun Glint Correction Methods. *Remote Sens.* **2019**, *11*, 2422. [CrossRef]
51. Hochberg, E.J.; Andréfouët, S.; Tyler, M.R. Sea Surface Correction of High Spatial Resolution Ikonos Images to Improve Bottom Mapping in Near-Shore Environments. *IEEE Trans Geosci Remote Sens.* **2003**, *41*, 1724–1729. [CrossRef]

52. Szostak, R.; Zimnoch, M.; Wachniew, P. *The Algorithm of Remote Sensing Thermal Imagery Calibration Dedicated for UAV-Based Hydrological Studies*; EGU General Assembly: Vienna, Austria, 2023. [CrossRef]
53. Aragon, B.; Johansen, K.; Parkes, S.; Malbeteau, Y.; Al-Mashharawi, S.; Al-Amoudi, T.; Andrade, C.F.; Turner, D.; Lucieer, A.; McCabe, M.F. A calibration procedure for field and UAV-based uncooled thermal infrared instruments. *Sensors* **2020**, *20*, 3316. [CrossRef]